Supporting Information

Combating Solvent Concentration Polarization for Ultrafast and Highly Stable Lithium Batteries at −60 °C

Zhijian Qiu,[ab] Yongpeng Cui,*[a] Lina Ge,[b] Wanning Xiong,[b] Zeyi Zhang,[a] Kaian Yang,[a] Yao Wang,*[c] Xiuli Gao,[b] Pengyun Liu,[b] Xuejin Li,[b] Qingzhong Xue,[b] Wei Xing,*[b]

[a] College of New Energy and Materials, State Key Laboratory of Heavy Oil Processing, China University of Petroleum (Beijing), Beijing, 102249, China

[b] School of Materials Science and Engineering, State Key Laboratory of Heavy Oil Processing, China University of Petroleum (East China), Qingdao 266580, China

[c] College of Science, State Key Laboratory of Heavy Oil Processing, China University of Petroleum (Beijing), Beijing, 102249 China

*Email: yongpengcui@cup.edu.cn

wangyao99@cup.edu.cn

xingwei@upc.edu.cn

Experimental Section

Preparation of Electrolyte Solutions. Ethylene carbonate (EC, 99.9%), fluoroethylene carbonate (FEC, 99.9%), difluoroethylene carbonate (DFEC, 99.9%), dimethyl carbonate (DMC, 99.9%), and lithium bis(fluorosulfonyl)imide (LiFSI, 99.9%) were purchased from Dodo Chemical Reagent Co. 2,2,2-Trifluoroethanol (TFEOH, 98%), aluminum chloride hexahydrate ($AlCl_3$, 98%), nitromethane (CH_3NO_2, 98%), and chlorobenzene (C_6H_5Cl, 98%) were purchased from Aladdin Reagent. Bis(2,2,2-trifluoroethyl) carbonate (TFEC) was synthesized via a branched-chain substitution of DMC under high-pressure conditions. In detail, 0.1 M DMC and 0.2 M TFEOH were mixed and added to 100 mL of C_6H_5Cl, followed by the addition of 0.1 M CH_3NO_2 and 0.1 M $AlCl_3$. After thorough mixing, the mixture underwent a homogeneous reaction at 60 ^{o}C for 12 h. Upon cooling, TFEC was obtained through Soxhlet extraction. All solvents were dehydrated using lithiated molecular sieves to a water content below 50 ppm. To prepare the low depolarized solvent-based electrolyte (LDSE), 0.01 M LiFSI was dissolved in 10 mL of a mixed solvent of EC:TFEC (1:1 by volume) at room temperature, followed by continuous stirring until the solution became clear. Following the same protocol, partially depolarized solvent-based electrolyte (PDSE) and high depolarized solvent-based electrolyte (HDSE) were prepared by dissolving 0.01 M LiFSI in 10 mL of a mixed solvent of FEC:TFEC (1:1 by volume) and DFEC:TFEC (1:1 by volume), respectively.

Preparation of Electrodes. Disodium rhodizonate (DSR), indigo carmine (IC), and metanil yellow (MY) were purchased from Aladdin Reagent. The synthesis of DSR was optimized based on a previously reported study.[1] Specifically, 200 mg of commercial DSR was dissolved in 250 mL of a mixed solvent of water and ethanol (2:1 by volume), followed by sonication and stirring for 30 min. Subsequently, 500 mL of ethanol was added to the solution under ultrasonication in an ice bath at 0 ^{o}C. The resulting precipitate was collected by suction filtration and dried in a vacuum oven at 60 ^{o}C for 12 h. To fabricate the DSR working electrodes, the active material (DSR), conductive carbon (Ketjenblack), and polyvinylidene fluoride (PVDF) binder were uniformly ground in a mass ratio of 7:2:1. The mixture was then dispersed in N-methyl-2-pyrrolidone (NMP) to form a slurry. This slurry was uniformly cast onto copper foil and subsequently dried under vacuum for 12 h to obtain the DSR working electrode. The areal mass loading of the active material was controlled at 2-3 mg cm^{-2}, unless stated otherwise. The IC and MY working electrodes were prepared following the same protocol as the DSR working electrode, but without the material optimization step.

Cell Assembly and Electrochemical Measurements. Li||Li symmetric cells, Li||DSR, and stainless steel (SS)||Li asymmetric cells were fabricated into CR2032-type coin cells, using lithium foil as the anode and Celgard 2500 (polypropylene, Φ19 mm) as the separator. The electrolyte volume in the coin cells was approximately 40 µL. The electrochemical stability window of the electrolyte was determined by linear sweep voltammetry (LSV) using an SS||Li asymmetric cell at a scan rate of 2 mV s^{-1} within a voltage range of 3 to 5.5 V. Cyclic voltammetry (CV) measurements were conducted on Li||DSR asymmetric cells to investigate the redox peaks at varying scan rates from 0.2 mV s^{-1} to 5 mV s^{-1}, within a voltage range of 1 to 3.5 V. Electrochemical impedance spectroscopy (EIS) was performed on Li||Li symmetric cells and Li||DSR asymmetric cells from 20 to −60 ^{o}C to measure the desolvation energy and electrochemical impedance. The tests were conducted in the frequency range of 10^{5} to 10^{-3} Hz with an amplitude of 10 mV. The distribution of relaxation time (DRT) analysis was performed by using DRT Tools. All the above tests were conducted using a Bio-logic VSP electrochemical workstation. Galvanostatic charge-discharge tests were performed at a current density of 0.1C (1C was defined as 350 mAh g^{-1}) within a voltage range of 1 to 3.5 V. Rate capability was tested at current densities from 1C to 20C, and cycling performance was evaluated at a current density of 2C from 20 to −60 ^{o}C. All charge-discharge tests were performed using the LANHE battery testing system.

Materials Characterization. Raman spectra were collected on a LabRAM HR800 spectrometer (HORIBA Jobin Yvon IBH Ltd.), using a 785 nm laser for electrolyte analysis. Nuclear Magnetic Resonance (NMR) measurements were conducted on an Ascend 600 MHz instrument (Bruker Co., Ltd.). Atomic Force Microscopy (AFM) and

Kelvin Probe Force Microscopy (KPFM) were performed using a Cypher VRS (Oxford Instruments). Time-of-Flight Secondary Ion Mass Spectrometry (ToF-SIMS) analyses were carried out on a PHI TOF NANO 3 instrument. Morphological characterization was performed using a scanning electron microscope (SEM, HITACHI Regulus8100). Longitudinal *in-situ* Raman spectroscopy was employed to characterize the concentration changes of solvents in the electrolyte during charge-discharge cycles by collecting the characteristic Raman peaks of the solvents using the X-Z mapping function of the LabRAM HR800 in an electrochemical *in-situ* cell (BJSCISTAR). *In-situ* Raman spectra of the electrodes were collected using the LabRAM HR800 to characterize the reversibility of the electrode by monitoring specific peaks.

Experimental Procedure for *In-situ* Raman Spectroscopy: The active material slurry was coated onto a porous current collector and dried. The *in-situ* Raman cell was then assembled in a glovebox, with the working electrode placed tightly against the optical window to ensure optimal focus. After sealing and electrolyte injection, the cell was allowed to stand for 12-h wetting period. The operating temperature of the cell was maintained at 20 ^{o}C or −20 ^{o}C. Raman measurements were performed in depth profiling mode using a 785 nm laser. The laser was focused on the sample surface, which was defined as the Z-axis zero (start point), with the scanning endpoint set to 4 µm above the surface. Galvanostatic cycling (0.2 C) was synchronized with the time-series acquisition of the Raman spectra.

Computational Methods. Molecular dynamics (MD) simulations were conducted using the GROMACS 2021.3 software package. All molecules were first subjected to geometry optimization and frequency calculations using Gaussian 16. Subsequently, Restrained Electrostatic Potential (RESP) charges and GAFF2 force field parameters were assigned via the Multiwfn program. For the DSR system, structural optimization and periodic charge calculations were performed with CP2K 2025.1, followed by the assignment of UFF force field parameters using Multiwfn. The simulation protocol involved three stages: (1) a 5-ns equilibration of the electrolyte solution in the NPT ensemble at 298.15 K to achieve equilibrium in both volume and molecular distribution; (2) a 5-ns pre-equilibration of the complete system in the NVT ensemble; and (3) a 5-ns production run, also in the NVT ensemble. During this final production stage, an external electric field was applied by setting a potential difference of 0.3 V across the simulation model, with the working electrode defined as the reference at 0 V. Trajectory data from this stage were collected for all subsequent analysis.[2, 3]

Table S1. The physical properties for these solvents.[4]

Solvent		Viscosity, mPa·s	Density, g cm^{-3}	Dielectric Constant
Ethylene Carbonate	EC	1.9	1.32	90.5
Fluoroethylene Carbonate	FEC	4.4	1.45	79.7
Difluoroethylene Carbonate	DFEC	2.7	1.52	35.4
Bis(2,2,2-trifluoroethyl) Carbonate	TFEC	0.4	1.51	4.4

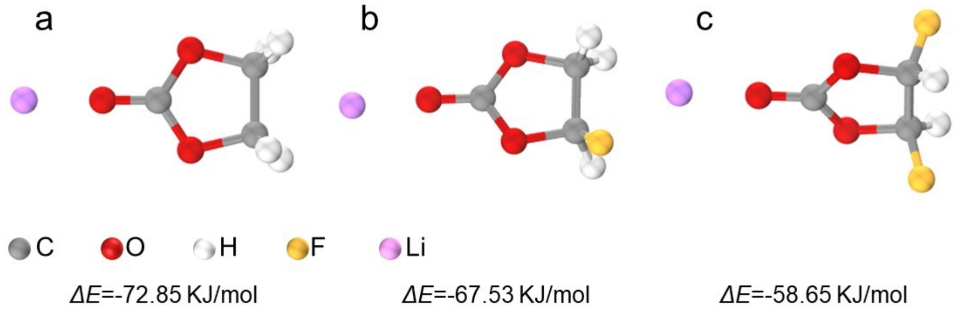

Figure S1. Binding energy between (a) ethylene carbonate (EC); (b) fluoroethylene carbonate (FEC); and (c) difluoroethylene carbonate (DFEC) solvent and Li^+. Note: low depolarized solvent: (EC); partially depolarized solvent: (FEC); high depolarized solvent (DFEC).

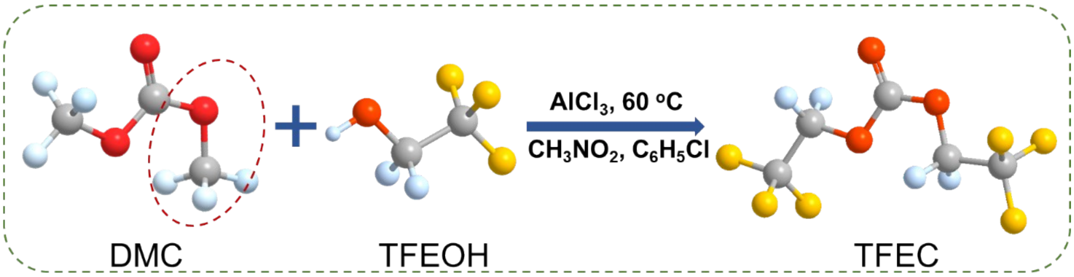

Figure S2. Scheme for the synthesis of the di(2,2,2-trifluoroethyl) carbonate solvent.

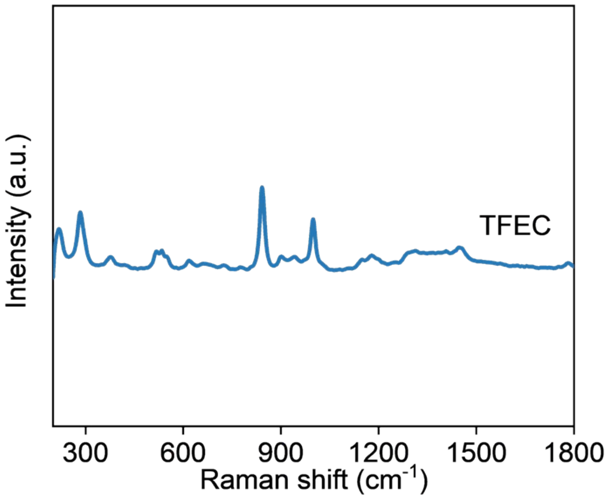

Figure S3. Raman spectroscopy of the di(2,2,2-trifluoroethyl) carbonate solvent.

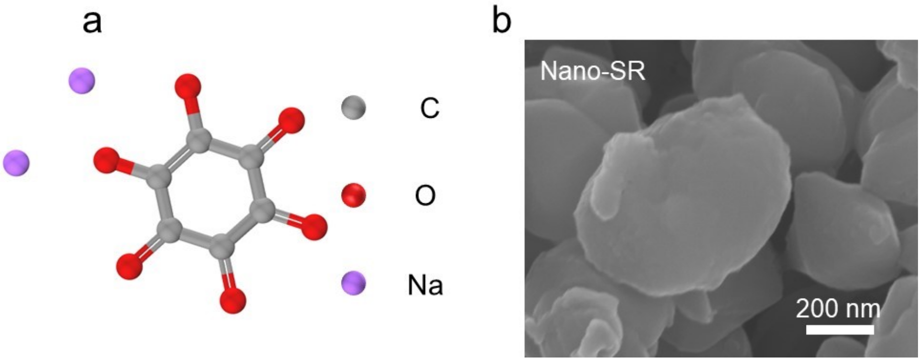

Figure S4. (a) Molecular structure of DSR and (b) SEM images of the DSR after solvent-mediated molecular self-assembly.

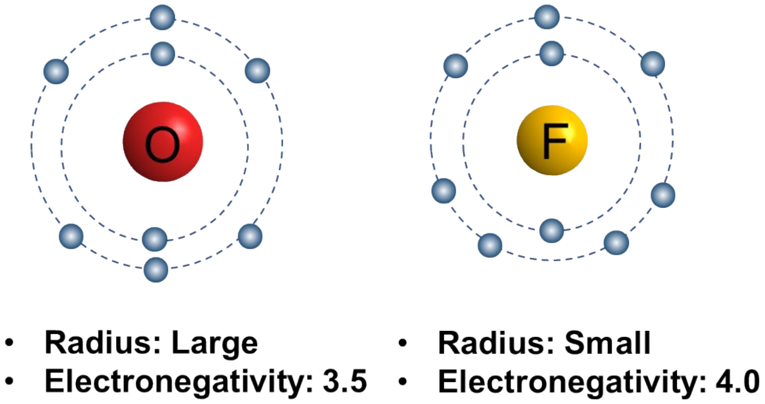

Figure S5. Comparison of the properties of oxygen atoms and fluorine atoms.[5, 6]

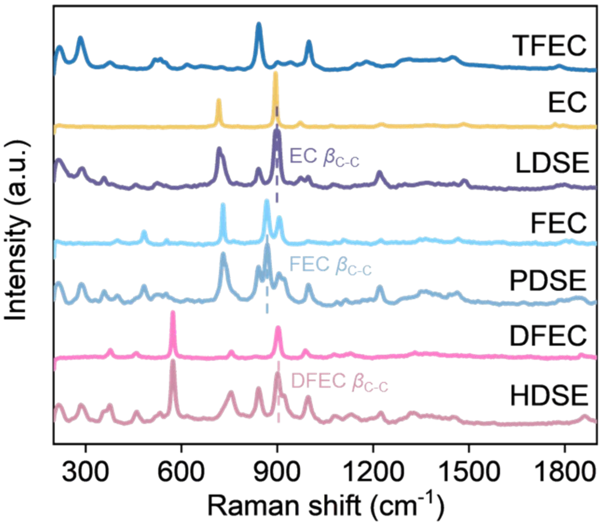

Figure S6. Raman spectra of β_{C-C} characteristic peaks for EC, FEC, and DFEC solvents in these three electrolyte systems.

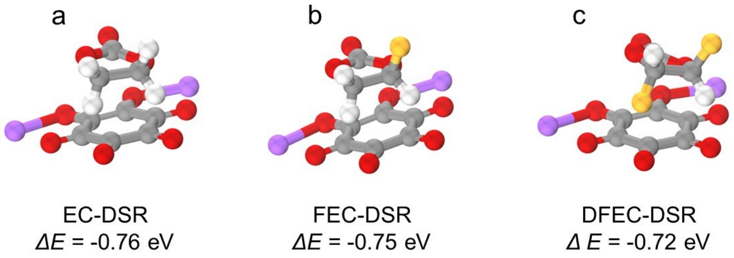

Figure S7. The binding energies between the electrode molecule (DSR) and the three solvents.

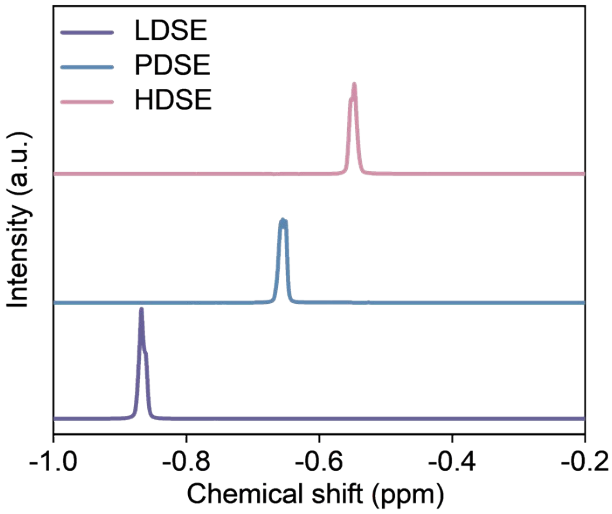

Figure S8. ^{7}Li NMR spectra of the LDSE, PDSE and HDSE electrolytes at room temperature.

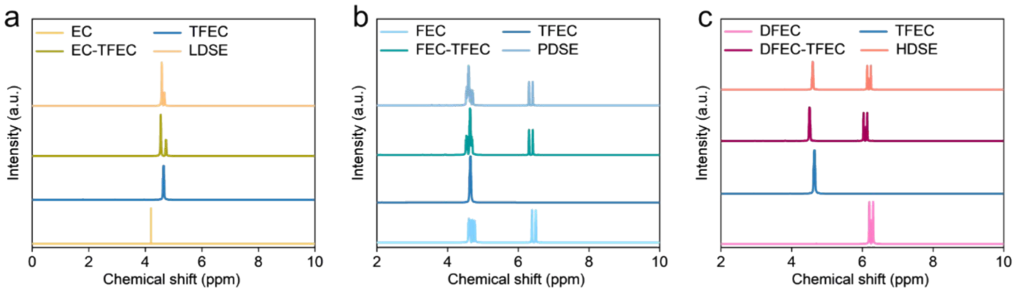

Figure S9. ^{1}H NMR spectra of the LDSE, PDSE and HDSE electrolytes at room temperature.

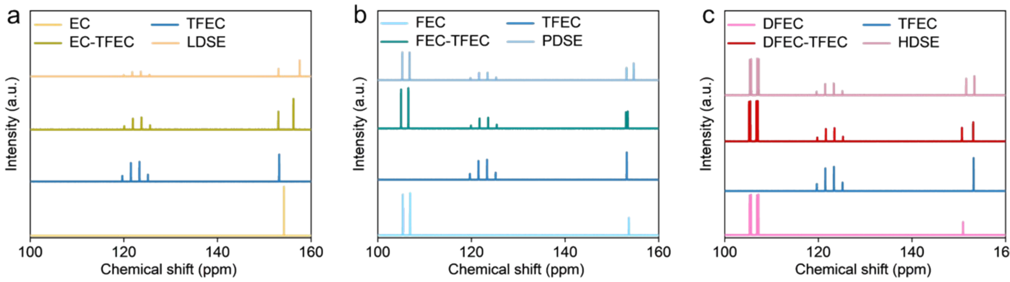

Figure S10. ^{13}C NMR spectra of the LDSE, PDSE and HDSE electrolytes at room temperature.

Note: The C=O groups interacting with Li^{+} are highly sensitive to the coordination environment. Notably, the ^{13}C signal in the HDSE exhibits a smaller chemical shift at ~178 ppm, confirming that the reduced solvent strength allows for easier anion participation in the Li^{+} solvation sheath.

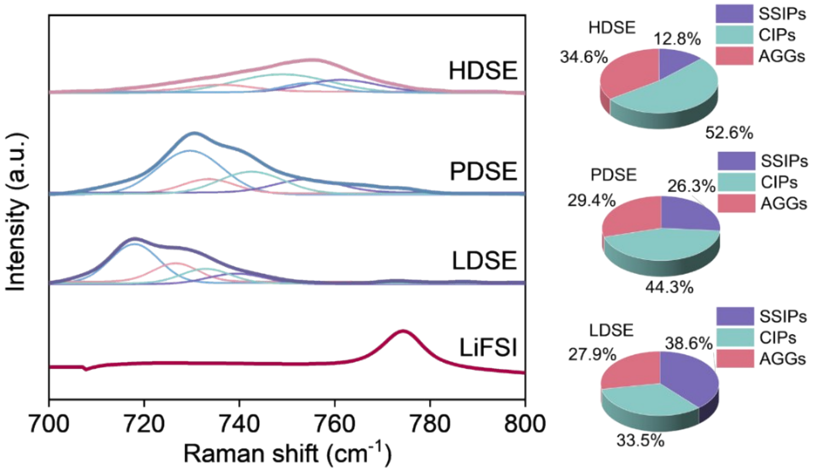

Figure S11. The shift of the S-N-S peak for the FSI^{-} anion in three different electrolytes.

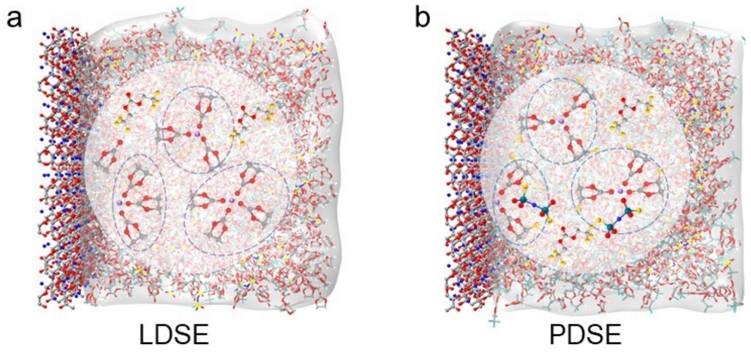

Figure S12. MD simulation of the LDSE and PDSE.

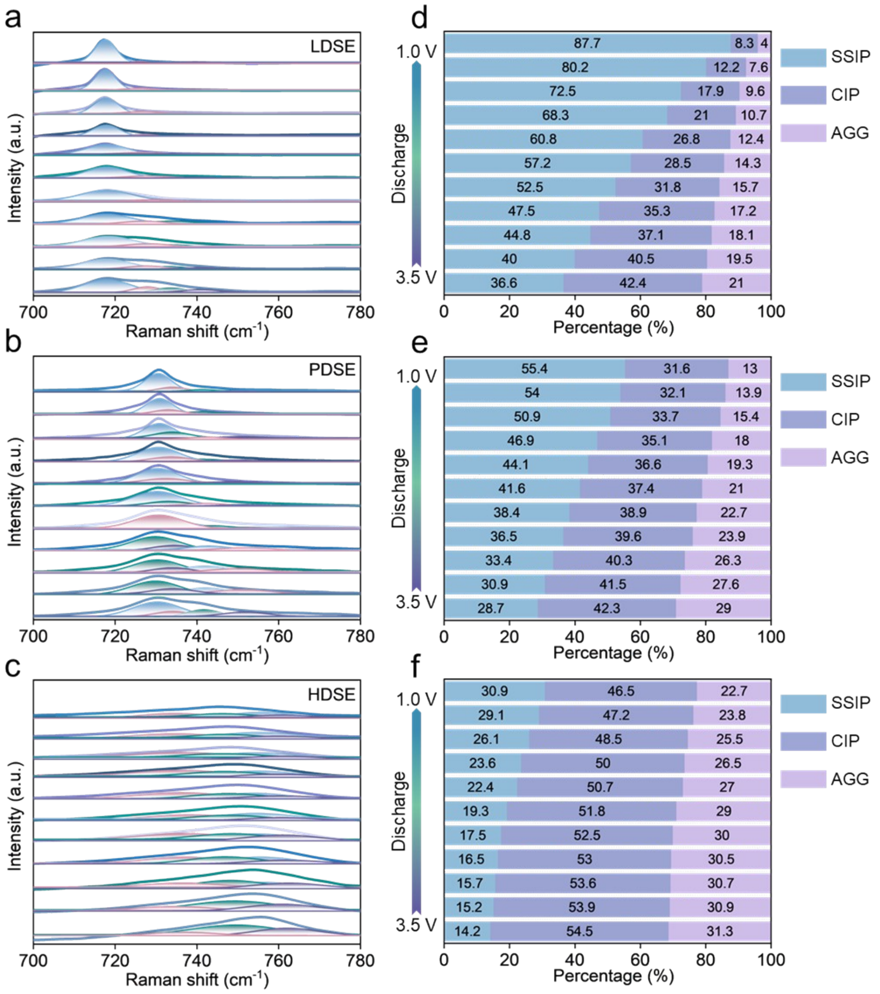

Figure S13. *In-situ* Raman spectra of Li||DSR cells using (a) LDSE, (b) PDSE and (c) HDSE during the discharge process at −20 ^{o}C and the proportions of SSIP, CIP, and AGG in the solvation structure.

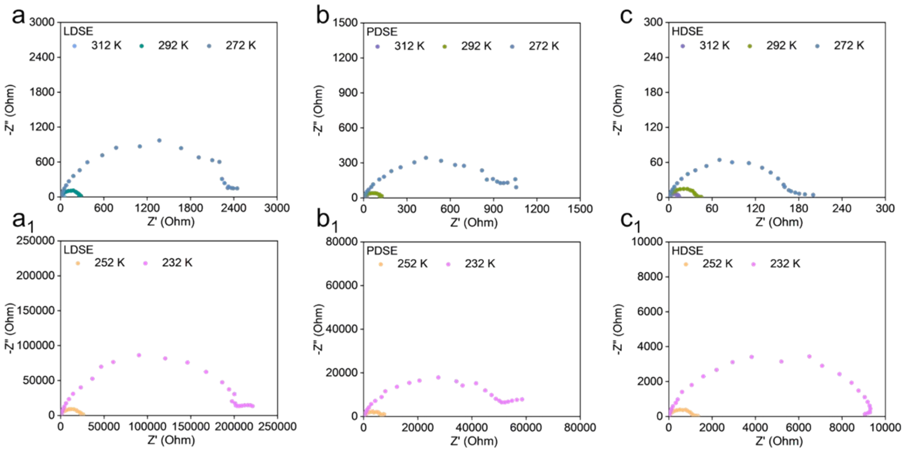

Figure S14. EIS of Li||Li cells using (a) LDSE, (b) PDSE, and (c) HDSE electrolytes at different temperatures.

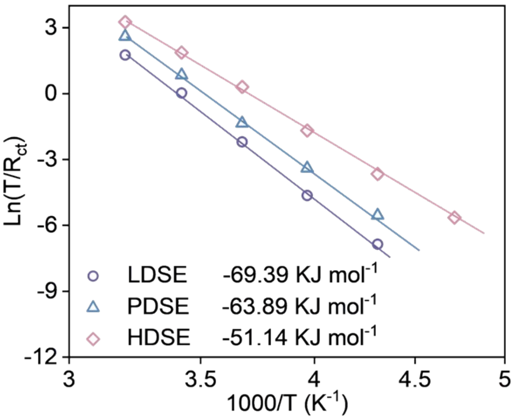

Figure S15. Arrhenius behavior in these electrolytes of the R_{ct} corresponding to Li^+ desolvation, obtained based on **Figure S14**.

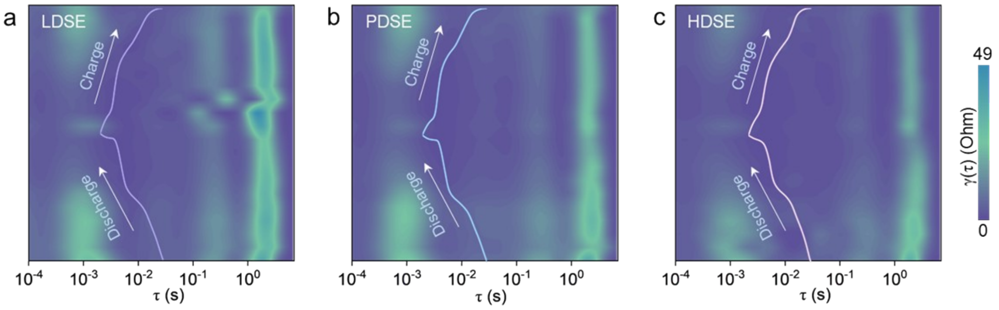

Figure S16. The DRT of the Li||DSR cells in (a) LDSE, (b) PDSE and (c) HDSE during the intercalation/de-intercalation of Li^+.

Note: In the LDSE system, the peaks corresponding to charge transfer and diffusion sustain high intensity as the discharge deepens, signifying the detrimental impact of solvent concentration polarization within the electric double layer on the interfacial kinetics of Li^+ desolvation. Conversely, the HDSE system exhibits shorter relaxation times and diminished peak intensities for these processes, which enables rapid ion migration and reaction kinetics.

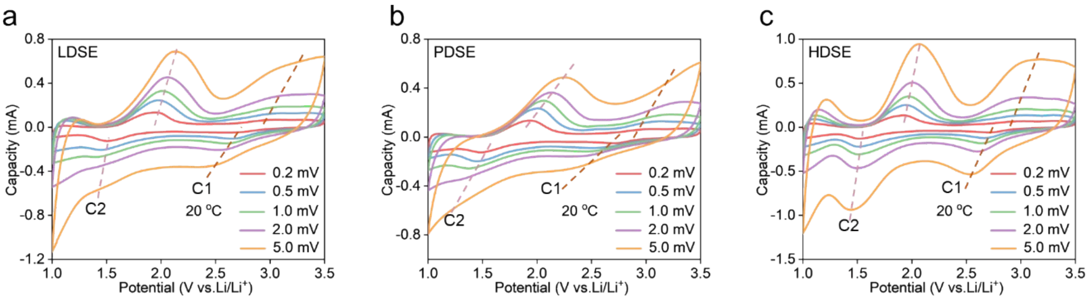

Figure S17. CV curves of Li||DSR cells using (a) LDSE, (b) PDSE, and (c) LDSE electrolytes at different scan rates.

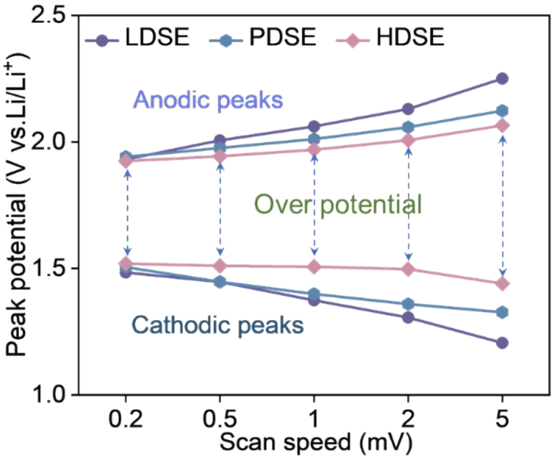

Figure S18. The scan rate dependence of Li^+ de-/intercalation overpotentials for Li||DSR cells.

Note: The DSR electrode undergoes stepwise lithium intercalation, which the C2 peak pair of Figure S17 is the key rate-determining step, and the overpotential is associated with this pair of peaks.

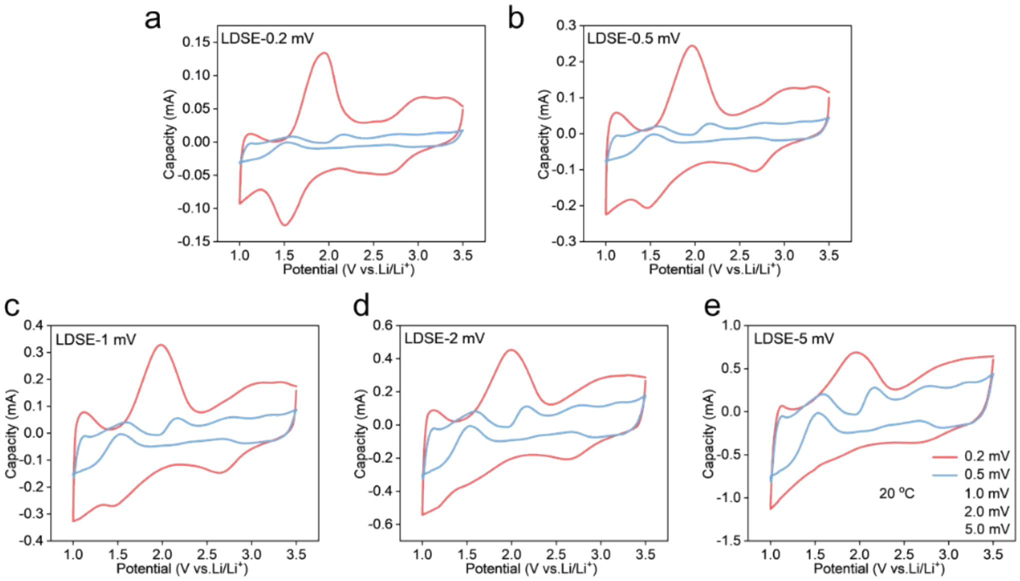

Figure S19. Pseudocapacitive contribution (calculated based on CV data) of Li||DSR cells based on the LDSE at different scan rates.

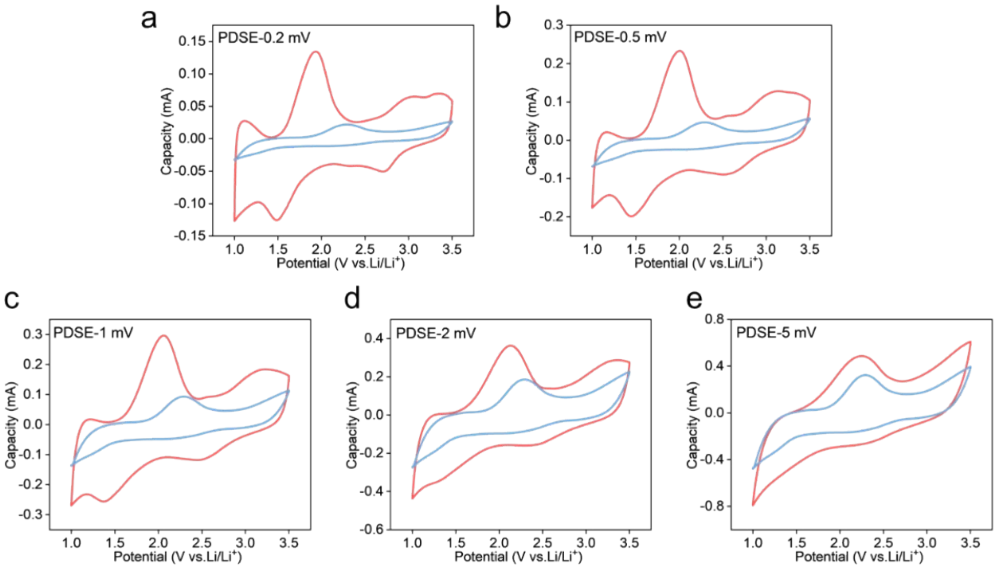

Figure S20. Pseudocapacitive contribution (calculated based on CV data) of Li||DSR cells based on the PDSE at different scan rates.

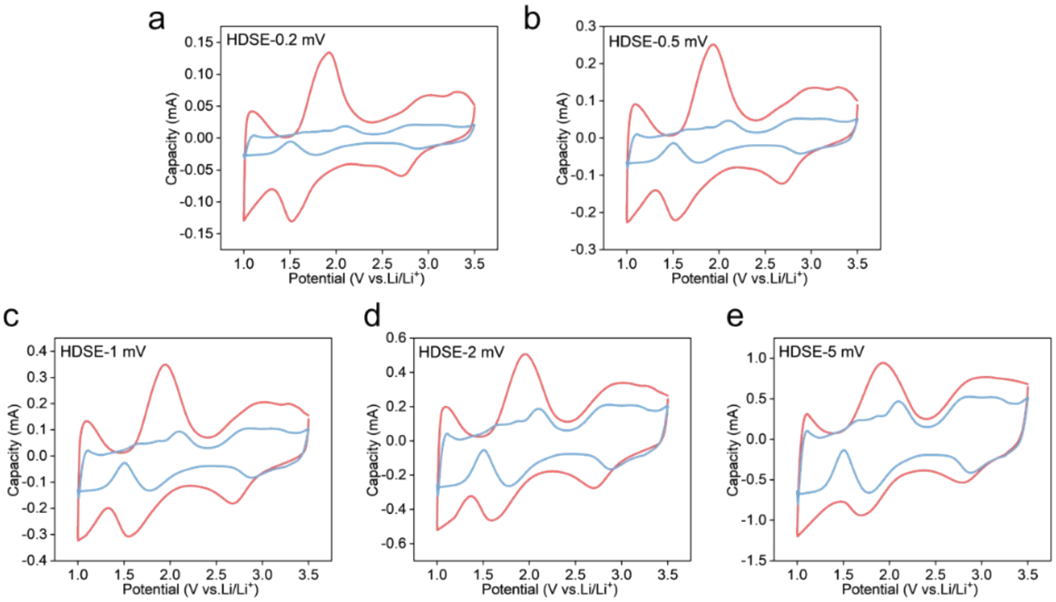

Figure S21. Pseudocapacitive contribution (calculated based on CV data) of Li||DSR cells based on the HDSE at different scan rates.

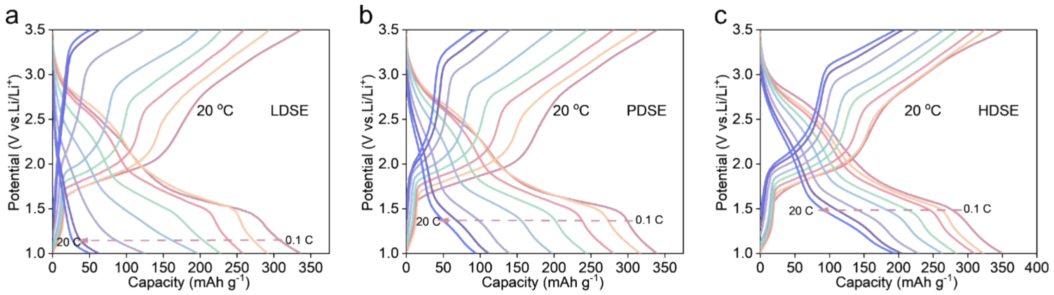

Figure S22. Charge and discharge curves of Li||DSR cells using (a) LDSE, (b) PDSE, and (c) HDSE electrolytes.

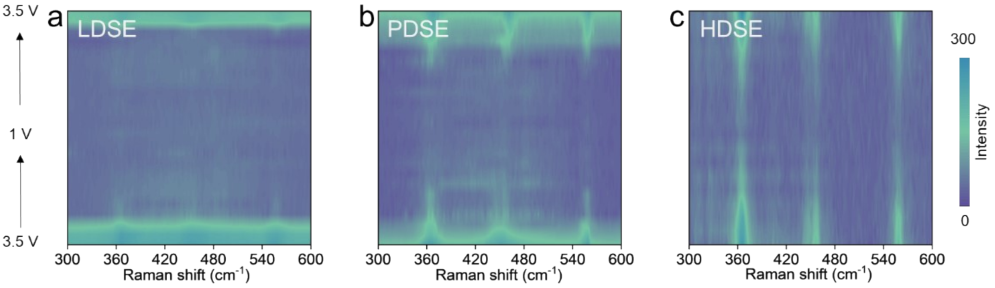

Figure S23. *In-situ* Raman showing the structural integrity and reaction reversibility of the the DSR electrode during the intercalation/de-intercalation of Li$^+$, using (a) LDSE, (b) PDSE, and (c) HDSE.

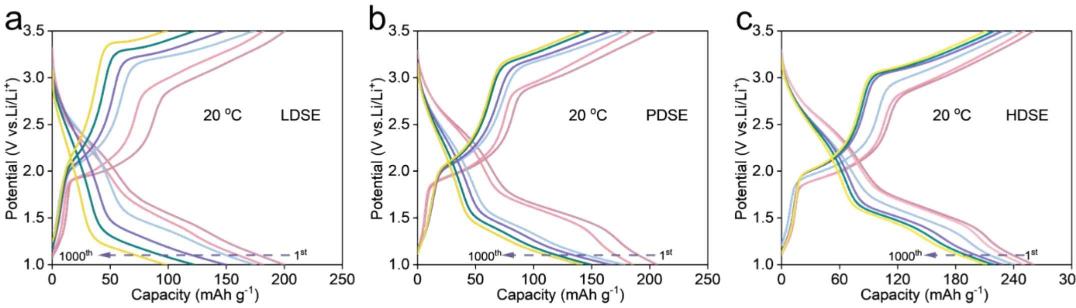

Figure S24. Voltage curves of Li||DSR cells using (a) LDSE, (b) PDSE, and (c) HDSE electrolytes at a current rate of 2C.

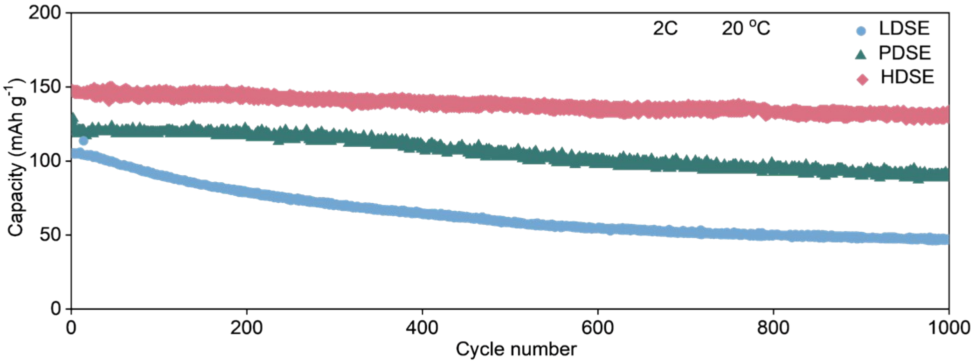

Figure S25. Cycling performance of Li||IC cells based on three electrolytes with a current rate of 2 C at 20 °C.

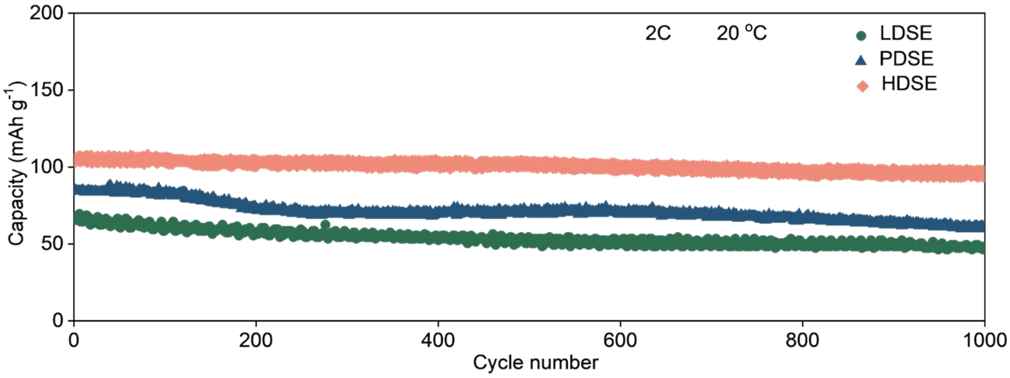

Figure S26. Cycling performance of Li||MY cells based on three electrolytes with a current rate of 2 C at 20 °C.

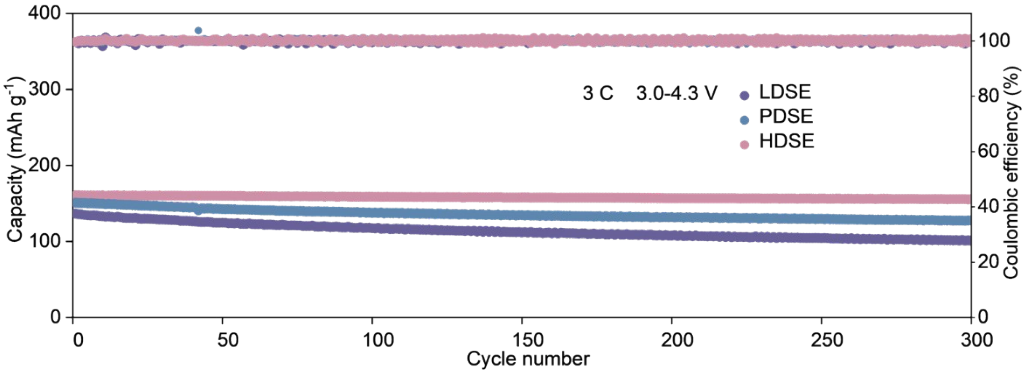

Figure S27. Cycling performance of Li||NCM811 cells based on three electrolytes with a current rate of 3 C at 20 °C.

Note: As shown in Figure S27, the Li||NCM811 cell using the HDSE system exhibits excellent cycling performance, with a capacity retention of 96.7% after 300 cycles. This is significantly higher than the 73.9% observed in the LDSE system.

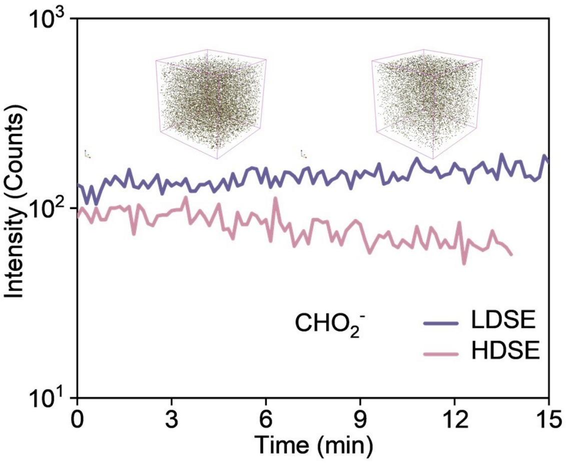

Figure S28. TOF-SIMS depth profiles and 3D reconstruction images (show in the insets) of CHO_2^- fragment in the EEI formed with the LDSE and HDSE.

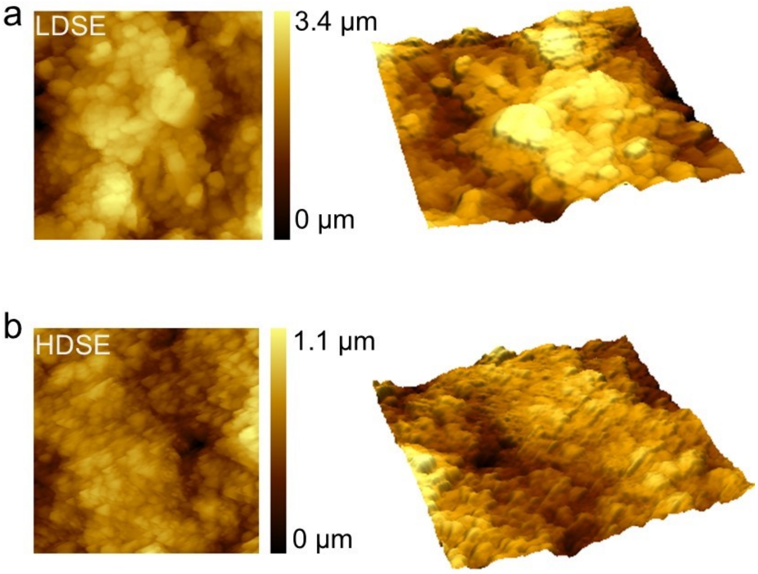

Figure S29. AFM morphology of EEI on the DSR electrode surface after cycling in (a) LDSE and (b) HDSE.

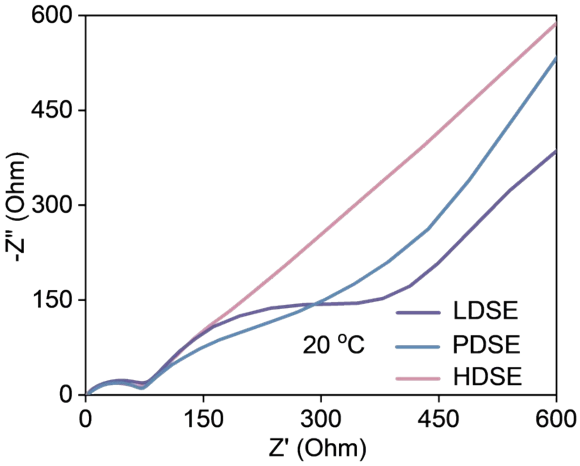

Figure S30. EIS results of Li||DSR cells after cycling in these electrolytes.

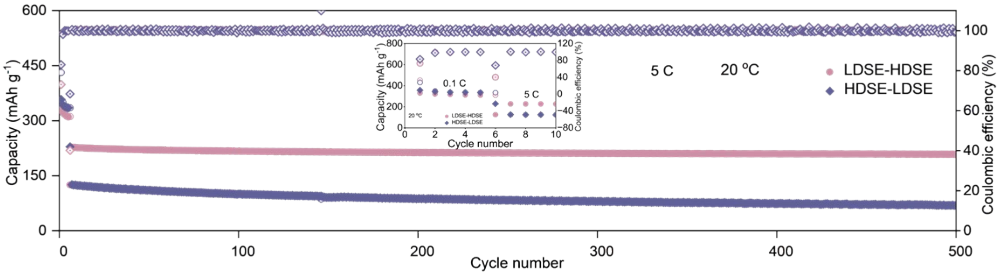

Figure S31. Comparative cycling performance of Li||DSR cells pre-cycled for 5 cycles in LDSE followed by long-term cycling in HDSE, versus those pre-cycled for 5 cycles in HDSE followed by long-term cycling in LDSE.

Note: Specifically, identical DSR electrodes are pre-cycled in LDSE and HDSE electrolytes for 5 cycles to construct the EEI, followed by disassembly and long-term cycling in the exchanged electrolytes, designated as LDSE-HDSE and HDSE-LDSE. The results demonstrate that although the HDSE-LDSE configuration avoids catastrophic rapid decay, its cycling performance remains significantly inferior to that of the LDSE-HDSE system.

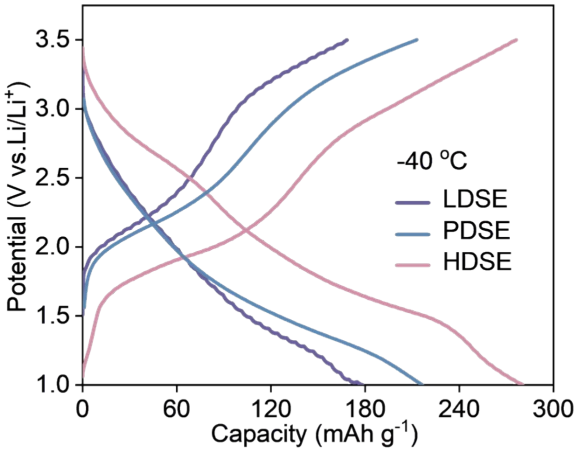

Figure S32. Charge-discharge curves of Li||DSR cells at −40 °C.

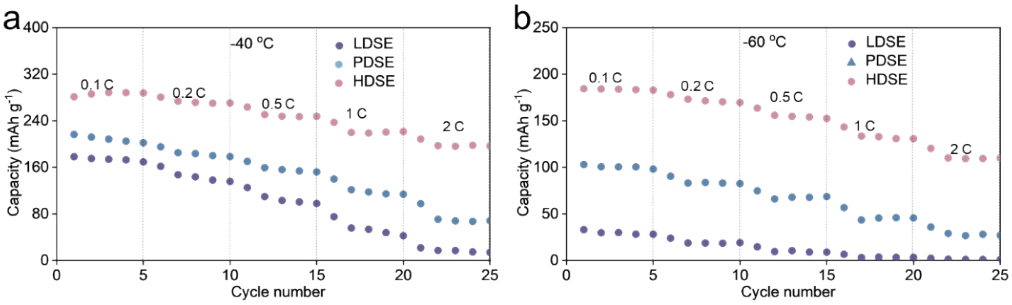

Figure S33. Rate performance of Li||DSR cells at (a) −40 °C and (b) −60 °C.

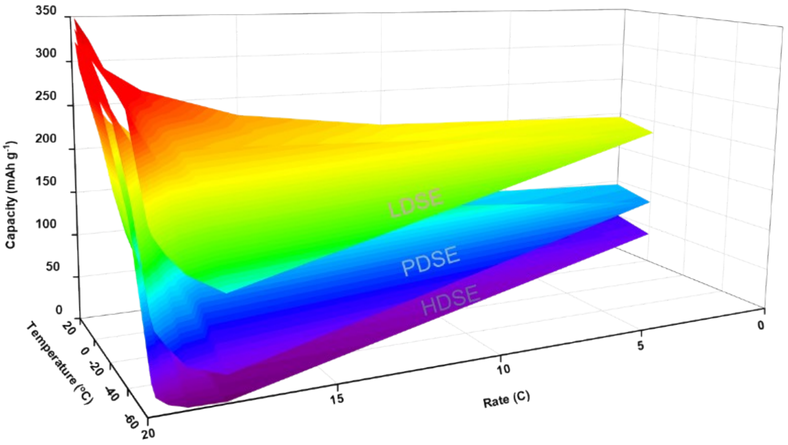

Figure S34. Comparison of rate-temperature relationships for Li||DSR cells based on three electrolytes.

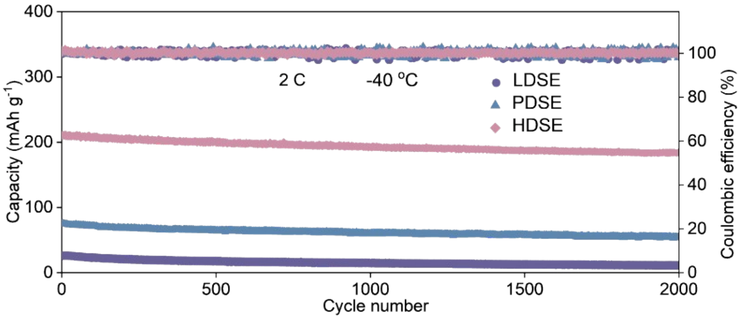

Figure S35. Cycle performance of Li||DSR cells based on three electrolytes at −40 °C.

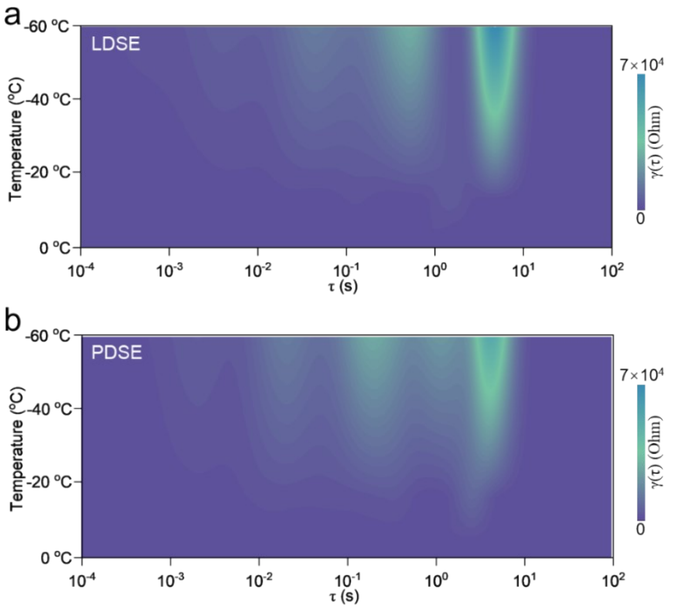

Figure S36. The DRT of the Li||DSR cells in (a) LDSE and (b) HDSE at different temperatures.

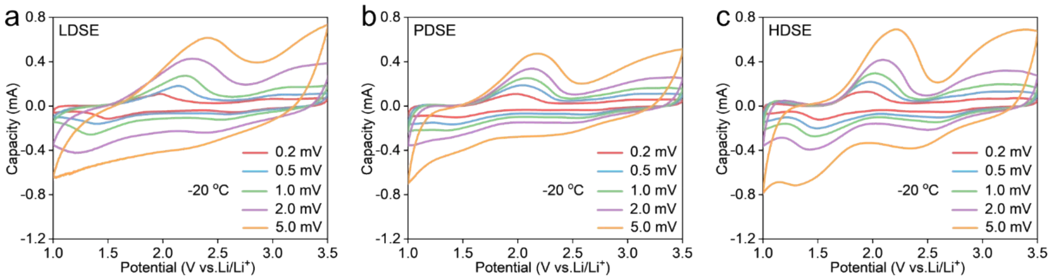

Figure S37. CV curves of Li||DSR cells with (a) LDSE, (b) PDSE and (c) HDSE systems with different scan rates at −20 °C.

References

1 X. Xu, S. Ren, H. Wu, H. Li, C. Ye, K. Davey, S.-Z. Qiao, *J. Am. Chem. Soc.*, 2024, **146**, 1619-1626.

2 X. Yin, B. Li, H. Liu, B. Wen, J. Liu, M. Bai, Y. Zhang, Y. Zhao, X. Cui, Y. Su, et al., *Joule*, 2025, **9**, 101823.

3 T. Lu, *J. Chem. Phys.*, 2024, **161**, 082503.

4 C. Wohlfarth, Static Dielectric Constants of Pure Liquids and Binary Liquid Mixtures, *Springer, Berlin*, 2015, **vol. IV/27**.

5 Y. Lu, Z. Yang, Q. Zhang, W. Xie, J. Chen, *J. Am. Chem. Soc.*, 2024, **146**, 1100-1108.

6 K. Xu, *Chem. Rev.*, 2014, **114**, 11503-11618.